Journal of
Materials Chemistry B

PAPER

Cite this: *J. Mater. Chem. B*, 2023, **11**, 7169

Investigation of the antibacterial properties of hyaluronic acid microneedles based on chitosan and MoS_2†

Wenzhen Du, Xiaodan Li, Manyue Zhang, Guixia Ling* and Peng Zhang *

Microneedle (MN) systems for painless transdermal drug delivery have been well developed over the past few years to overcome the problems of subcutaneous injections. Hyaluronic acid (HA) is a glycosaminoglycan that exists widely in living organisms, and chitosan (CS) is the only basic polysaccharide among natural polysaccharides, both of which have good biodegradability. Molybdenum sulfide (MoS_2) is a typical layered transition metal disulfide with a two-dimensional structure and many unique physicochemical properties. However, its applicability in antimicrobial MNs is unknown. Therefore, in this paper, the antibacterial properties of the nanocomposites formed by MoS_2 for MN preparation were investigated by combining the carbohydrate CS with antibacterial properties. The mechanical properties, irritation and blood compatibility of the prepared dissolving HA MN patches were investigated. Finally, the antibacterial properties of the composite MNs against *Escherichia coli* and *Staphylococcus aureus* were studied *in vitro* to evaluate the antibacterial properties of the developed antibacterial nanocomposite-loaded MNs. In addition, the results of the *in vivo* wound healing experiments showed that the dissolving antimicrobial MNs we prepared had a potential therapeutic effect on wound healing.

Received 6th April 2023,
Accepted 6th June 2023

DOI: 10.1039/d3tb00755c

rsc.li/materials-b

1. Introduction

The development of society means that people's living standards improve continuously, people pay more and more attention to a healthy quality of life, and the safety requirements for products have greatly increased, so the demand for antibacterial products has also increased, and the development of antibacterial products is necessary. Furthermore, with the emergence of resistance to existing antibiotics,[1] the development of alternative antibacterial agents is urgent. As a new type of antibacterial agent, nanomaterials have the advantage of high bactericidal efficiency without causing the development of drug resistance and are important alternative therapeutic agents for existing antibacterial agents.[2,3] In the past decade, there have been many studies on 2D nanomaterials such as graphene oxide (GO),[4] carbon nanotubes (CNTs), *etc.* The prosperity of 2D materials has made many 2D materials become reliable candidates for nanomedicines.[5] In particular, MoS_2 nanosheets, as an emerging 2D material with stable and unique physicochemical properties,[6] can be applied in tissue engineering[7] and cancer treatment,[8] and as antibacterial agents[9] and in many other biomedical applications. MoS_2 is a layered structure material with good chemical and thermal stability, rich natural content, low friction coefficient,[10] good catalytic activity, large surface area, easy functionalization, and the composition of the S–Mo–S atomic layer through weak van der Waals force interactions, and is considered as a graphene-like nanomaterial. Mo elements and S elements are essential for the survival of human beings, animals, and plants. Therefore, compared with other chalcogenide compounds of transition metal materials,[11] MoS_2 nanomaterials have better biological compatibility in biological applications such as cell imaging and targeted drug transportation.

Nanoscale MoS_2 films have negative charges and can be used for a variety of surface modifications, and their easily functionalized surfaces make them a wide range of nanoplatforms for biomedical applications. MoS_2 may have great potential against drug-resistant bacteria by appropriate surface modification or antimicrobial loading. It has been proved that MoS_2 nanosheets have antibacterial activity at a certain concentration,[12] and the antibacterial properties of MoS_2 materials have also been reported in photothermal therapy and photodynamic therapy.[13–16] Moreover, several functional nanocomposites have been reported for antimicrobial use.[17]

In recent years, biopolymer hybrid nanocomposites have gradually become a research hotspot in the fields of biomedicine, polymer engineering, and electrochemistry.[18] Among them,

---

Wuya College of Innovation, Shenyang Pharmaceutical University, No. 103, Wenhua Road, Shenyang 110016, China. E-mail: zhangpengspu@163.com, pharlab@163.com

† Electronic supplementary information (ESI) available. See DOI: **https://doi.org/10.1039/d3tb00755c**

natural polymers are important materials for realizing green chemistry due to their biodegradability, nontoxicity, and good biocompatibility. Naturally available biopolymers play a significant role in the field of medicine. Chitosan (CS, the structure is shown in Fig. S1, ESI†) is a naturally biodegradable cationic linear polysaccharide containing active amino and hydroxyl groups, which is second only to cellulose in abundance in nature. Its own positive charge can interact with the negatively charged cell wall of bacteria to effectively play an antibacterial role. In addition, CS can inhibit the formation of a bacterial biofilm, whose antibacterial properties have always been a research direction of great interest.[19] In recent years, nanocomposites based on MoS_2 and CS have been widely studied in the field of medicine as a new type of antibacterial material. CS–MoS_2 not only inherits the excellent performance of chitosan but also has the sulfur-rich surface of MoS_2, which makes it have a large adsorption capacity.[20] Combining MoS_2 with CS, a natural cationic polysaccharide with antibacterial properties can achieve enhanced antibacterial efficiency and dispersion stability,[21] and CS enhances the bactericidal efficacy by changing the surface charge of nanomaterials. The positively charged CS enhances the interaction of MoS_2 with the bacterial membrane, allowing it to adhere efficiently to the bacterial membranes. However, the introduction of this complex into MNs has not been explored.

MNs are an array of micron-sized needles[22] that can penetrate the stratum corneum without contacting nerve fibers and blood vessels located in the epidermis and dermis,[23] which can provide a continuous and controlled way to deliver therapeutic agents to specific sites and effectively overcome the shortcomings of traditional drug delivery methods,[24–26] and are a new dosage form that is convenient for the topical application of antibacterial agents. The development of MNs provides a low-cost, topical, painless, environmentally friendly, and patient-compliant drug delivery method.[27,28] The thickness of the bacterial biofilm is known to be up to several hundred micrometers, the appropriate MN length can destroy the physical barrier of bacteria and the large specific surface area can realize the effective delivery of antibacterial agents. Currently, MNs have been recognized as an effective minimally invasive treatment tool for bacterial biofilms. MNs with antibacterial properties have been used to treat diabetic wounds,[29] staphylococcal infection-induced chronic wounds,[30] and hair regeneration.[31] However, cavities created by MN administration made of non-biodegradable materials such as stainless steel may lead to mechanical damage to the administration site as well as microbial infection. The selection of matrix materials with good biocompatibility for the preparation of MNs can well avoid potentially serious side effects. Therefore, in this study, advanced polysaccharide HA was used as the main matrix for the preparation of antibacterial and dissolving microneedles, and polyvinylpyrrolidone K30 (PVP K30), which was officially approved by the national pharmaceutical administration, was used as an auxiliary material. In addition, the matrix materials we selected are all water-soluble, so the antibacterial agent can be released along with the dissolution of the MNs after the dissolving MNs are inserted into the skin. This also avoids the need to dispose of sharp biohazardous tip waste.

General dissolving MNs have the disadvantages of being susceptible to bacterial infection and inconvenient to store, with the potential to increase the risk of skin infections. Therefore, the development of dissolving MNs with good biocompatibility and better antibacterial ability is necessary. In this work, we aim to develop layered biopolymer hybrid nanocomposites with better antibacterial effects and combine them with MNs to prepare a dissolving antibacterial MN loaded with nanocomposites as antibacterial agents. Taking a lead from previous research studies,[32] we prepared CS–MoS_2 hybrid nanocomposites by the hydrothermal method under mild and environmentally friendly conditions and characterized their structural and morphological properties using suitable analytical techniques. In addition, the antibacterial activity of the dissolving HA MNs prepared based on CS and MoS_2 against Gram-positive and Gram-negative bacteria was also tested. Fig. 1b shows the process of loading a CS–MoS_2 complex into MNs for wound antibacterial and wound healing. The results showed that these MNs not only possessed good mechanical properties and desirable antibacterial activity but also exhibited good performance in blood compatibility. This suggests that CS–MoS_2-loaded dissolving MNs can break through the defects of traditional microneedles that are prone to infection, providing a promising perspective for the study of topical transdermal drug delivery in humans.

2. Materials and methods

2.1. Materials

Hyaluronic acid (HA) (M_w = 20–400 000 Da), nano molybdenum disulfide (MoS_2, ≥99.5%, 100 nm) and chitosan (CS) (M_w = 300 000 Da) were obtained from Shanghai Macklin Biochemical Co., Ltd. MH Broth was purchased from Haibo Biotechnology Co., Ltd. Agar (powder) was purchased from KERMEL. Polyvinylpyrrolidone K30 (PVP K30) was purchased from Tianjin Bodi Chemical Co., Ltd. Acetic acid (AR, 99.5%) was obtained from Tianjin Damao Chemical Reagent Factory. *S. aureus* and *E. coli* were purchased from Beijing Preservation Biotechnology Co., Ltd. Wahaha water was provided by Hangzhou Wahaha Group Co., Ltd.

2.2. Synthesis of CS–MoS_2 nanocomposites

CS–MoS_2 was synthesized by a hydrothermal liquid phase exfoliation method. The synthesis process of CS–MoS_2 hybrid nanocomposites is divided into two steps.[33,34] First, 50 mg (0.1% w/v) of CS was dissolved in 50 mL of 1% acetic acid solution by magnetic stirring. Then, 25 mg (0.05% w/v) of MoS_2 were added to the dissolved CS solution. The reactants were then sonicated for 5 h to form a MoS_2-dispersed CS (0.05 : 0.1% w/v ratio) matrix. Under ultrasonic conditions, the aggregated MoS_2 particles fall off to form relatively uniform MoS_2 nanosheets. Finally, the final mixture was centrifuged (6000 rpm, 15 min), which could separate a large amount of unstripped MoS_2 particles from the product in the reaction mixture. The products obtained after centrifugation were dried to obtain the CS–MoS_2 hybrid

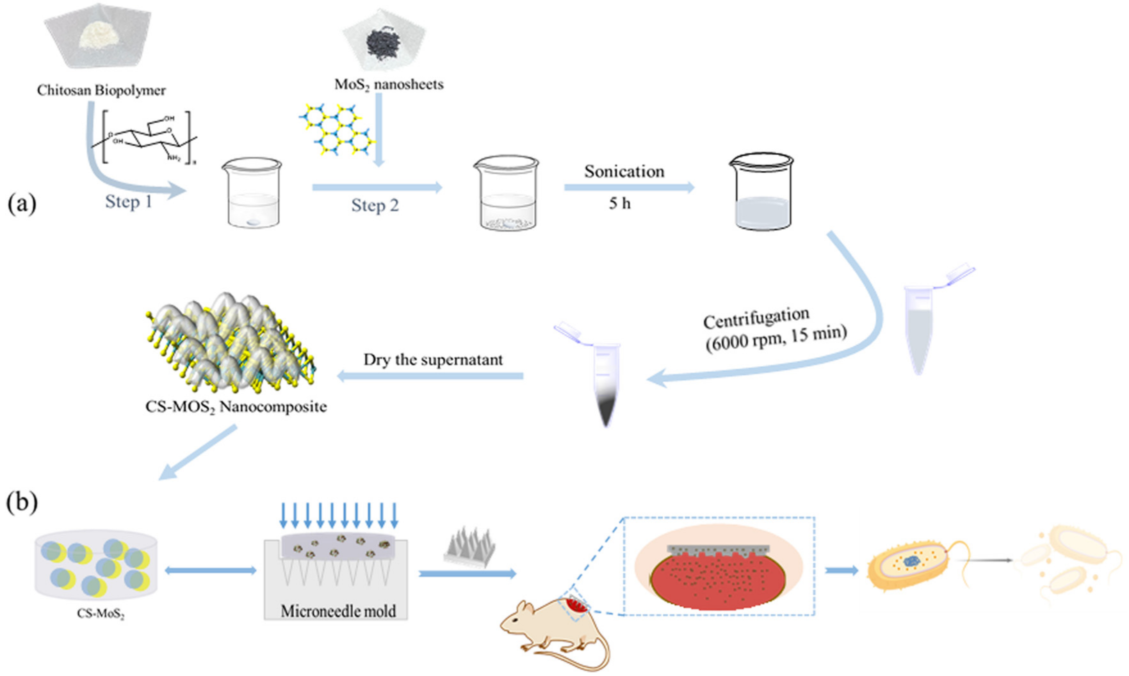

Fig. 1 The synthesis process of the CS–MoS_2 nanocomposite (a); the preparation process and the schematic diagram of the effect of CS–MoS_2 MN on the wound (b).

nanocomposite. The synthetic route of the nanocomposite is shown in Fig. 1a.

2.3. Characterization of CS–MoS_2 nanocomposites

Crystalline infrared (IR) spectra of CS–MoS_2 hybrid nanocomposites were obtained using a Thermo Scientific Nicolet iS20 model Fourier transform infrared (FTIR) spectrometer in the analytical range of 4000–400 cm^{-1}. The absorption spectrum of CS–MoS_2 was analyzed by ultraviolet-visible spectroscopy (UV-Vis), obtained using a Shimadzu UV-3600 UV-Vis spectrophotometer. Surface morphology and particle size were examined by scanning electron microscopy (SEM, Oxford x-max (ZEISS MERLIN Compact)). The surface functionalization of CS was further confirmed by zeta potential measurement of the complex using a Malvern particle sizer.

2.4. Preparation of blank MNs

MNs fabrication was performed using silicone molds and PDMS molds. The HA pregel was obtained by pre-dissolving the HA powder in an aqueous solution, and a certain proportion of polyvinylpyrrolidone was added to the HA solution to improve the appearance and mechanical properties of the prepared MNs. The obtained HA pregel was filled into the conical microcavity of the mold, allowed to stand for 5 min (as shown in Fig. 1b, without CS–MoS_2 solution), and then centrifuged at 3000 rpm for 10 min to fill the needle tips. The MN mold with a matrix gel was dried at room temperature for 24 h and demolded for storage. The mechanical properties of MNs prepared from different concentrations of HA solutions were investigated, and the most suitable concentrations were screened for the preparation of MNs (Fig. S2 and S3, ESI†). A certain proportion of polyvinylpyrrolidone was added to the HA solution to improve the mechanical properties. The MN prepared using a HA pregel with a concentration of 10% has good appearance and mechanical properties and has a relatively simple and convenient preparation process.

2.5. Preparation of CS–MoS_2 MNs

Firstly, CS–MoS_2 solutions with concentrations of 64, 128, 256, and 512 μg mL^{-1} were prepared, and then PVP K30 and HA were dissolved in CS–MoS_2 solution, and then magnetically stirred for 30 min to obtain well-mixed pre-gels containing different concentrations of CS–MoS_2. The pregel used to prepare the MNs was completely filled into the conical microcavity of the mold for 5 min under vacuum and centrifuged at 3000 rpm for 10 min to fully fill the needle tips (Fig. 1b). The microneedle molds with a matrix gel were dried at room temperature for 24 h, then the MNs were peeled from the molds and stored in a desiccator until further use.

2.6. Characterization of MNs

2.6.1. Morphological representation. The microstructure of the CS–MoS_2 composite was investigated using a scanning electron microscope (SEM, Oxford x-max (ZEISS MERLIN Compact)). The fabricated MNs were visualized with digital optical microscopy and SEM. The MN patch consists of 225 (15 × 15) complete and continuous needle arrays, each needle in the shape of a quadrangular pyramid, 600 μm high, 280 μm wide at the base, and spaced 800 μm apart. The morphology of the CS–MoS_2 MNs was observed from different angles at different magnifications with a digital optical microscope and SEM, respectively.

2.6.2. Mechanical property investigation. The mechanical properties of the HA MNs were investigated by using aluminum foil paper. The MN patch was pressed into aluminum foil with appropriate force, and the holes left by the puncture were observed with light to evaluate the mechanical properties of the MNs.

2.6.3. Skin puncture test. The puncture performance of MNs was investigated by using pig skin *in vitro*. After the pig skin was thawed, the surface water was removed with filter paper. Then, the skin was spread on the filter paper with the cuticle facing outward, and the MNs were pressed vertically with a certain intensity for 30 s. Then the MNs were pulled out. The skin was stained with a certain concentration of trypan blue solution for 10 min and the trypan blue solution removed from the skin surface, then the stained skin was observed and photographed, the holes left on the surface of the pig skin were counted and the puncture rate was calculated. The higher the puncture rate, the better the mechanical properties. The puncture rate was calculated according to the following formula:

$$\text{Puncture rate } (\%) = \frac{A_{\text{recorded}}}{A_{\text{original}}} \times 100\%$$

where A_{recorded} is the number of recorded microneedle holes; A_{original} is the number of original microneedle tips.

2.6.4. Skin healing test. The skin healing at the puncture site after MN skin puncture was evaluated by experiments on isolated pig skin and *in vivo* rat skin.[35] The frozen pig skin was taken and soaked in physiological saline. After the pig skin was thawed, the surface water was removed with filter paper, then the skin was spread on the filter paper, with the cuticle facing outward, the microneedle was pressed vertically with a certain strength for 30 s, and the MNs were pulled out. The punctured site was photographed and recorded at different time points. The living skin has better self-healing properties. After the SD rats were raised normally for 14 days, most of the longer hairs of the rats were trimmed with scissors, and then depilatory cream was evenly applied to the back skin of the rats for 3 min. The application time was properly lengthened or shortened according to the situation to avoid burning the rats' skin. Finally, wipe with warm water to remove the depilatory cream and the shed hair, and observe the back of the rat. When the skin of the rat was in good condition, the MN patch was pierced vertically into the skin of the back of the rat with an appropriate force, and the patch was removed after 30 s. At the same time, the camera was used to take pictures at different time points to record the healing process of the skin.

2.6.5. Solubility study. The MNs were inserted into the isolated pig skin and the skin of live rats, respectively, and the dissolution of the needle tips was observed under a microscope after maintaining for different times to investigate the dissolution of the MNs *in vitro* and *in vivo*.

2.6.6. Blood compatibility test. The hemolytic activity of the complexes was determined with reference to existing experiments to study their hemocompatibility.[36] First, solutions containing different concentrations of CS–MoS_2 were prepared as the solution to be tested for studying the blood compatibility of the nanocomposite. Then, the MN pregels loaded with different concentrations of CS–MoS_2 complexes were leached with physiological saline to obtain leaching solutions of different concentrations, and the leaching solution passed through a 0.22 μm filter. Then, the solution after filtration and the solution to be tested in the first step were incubated with rat red blood cells (RBC, 2% v/v) for 1 h at 37 °C. The saline-treated suspension was used as a negative control, while the suspension treated with Wahaha water was used as a positive control. Three replicate samples were provided for each group. After incubation, the incubations were centrifuged at 13 000 rpm for 5 min, and the OD value of the supernatant was measured at 545 nm. The hemolysis ratio was calculated according to the following formula:

$$\text{Hemolysis ratio } (\%) = \frac{\text{OD}_{\text{sample}} - \text{OD}_{\text{negative}}}{\text{OD}_{\text{positive}} - \text{OD}_{\text{negative}}} \times 100\%$$

2.7. Antibacterial performance evaluation

Staphylococcus aureus (*S. aureus*) and *Escherichia coli* (*E. coli*) were used as experimental strains. The frozen *S. aureus* and *E. coli* were coated and inoculated in MH liquid medium, and the culture was shaken at 37 °C for an appropriate time until the turbidity was equivalent to that of the McFarland turbidimetric tube No. 0.5 (the OD value is approximately equivalent to 0.1). And then diluted with sterile physiological saline at a ratio of 1 : 10, and 100 μL of the bacterial solution were drawn from each dilution level, spread evenly on agar plates, and incubated at 37 °C for 24 h, and then according to the Chinese national standard GB 4789.2, the bacteria were counted, the bacterial concentration of the original bacterial solution was calculated, and the bacterial solution of appropriate concentration was further prepared for subsequent antibacterial experiments.

The minimum inhibitory concentration (MIC) and minimum bactericidal concentration (MBC) of the CS–MoS_2 complex against *S. aureus* and *E. coli* were investigated by the double dilution method, respectively. According to the experimental results of MIC and MBC, appropriate concentrations were set to investigate the antibacterial effect of the three materials CS, MoS_2, and CS–MoS_2. The bacterial suspensions of *E. coli* and *S. aureus* were co-cultured with MN patches loaded with different concentrations of CS–MoS_2 in a constant temperature shaker at 37 °C, and the bacterial growth curves were drawn to reflect the changes in the bacterial concentration in the bacterial suspension. The sterilizing rate of the prepared MNs containing different concentrations of CS–MoS_2 was investigated by the co-culture experiment, *E. coli* and *S. aureus* were cultured with HA MNs containing different concentrations of CS–MoS_2 for 6 h, and 10 μL of culture medium was absorbed and coated on an agar plate. After 24 h of culture, the viable bacteria on the plate were counted and the bactericidal rate was calculated. All experiments were performed in at least triplicate.

2.8. Wound healing experiment

Mature SD rats were depilated, and surgical scissors were used to cut a wound with an area of about 1 cm^2 on the skin of the backs of the rats after the skin returned to normal. 10 μL of

E. coli and *S. aureus* mixture was applied to the wound for 2 min and then scrubbed with normal saline for 1 min to complete the establishment of the wound model. Then the rats treated with MN were used as the experimental group, and the rats without MN treatment were used as the control group, *n* = 3. All rats were reared under the same conditions, and the wounds were photographed and compared on different days.

3. Results and discussion

3.1. Morphological characterization

The morphology of the synthesized CS–MoS_2 and the original MoS_2 were characterized by SEM. SEM results showed that the prepared CS–MoS_2 has a typical layered structure (Fig. 2a), which was different from the original flake MoS_2 (Fig. 2b), indicating successful functionalization. It could be seen from the image that modified MoS_2 has a smaller size (about 100 nm in size).

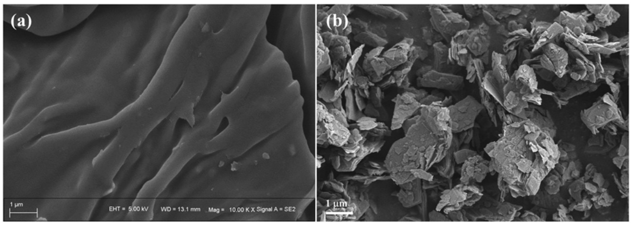

Fig. 2 SEM images of the prepared CS–MoS_2 (a) and the original MoS_2 (b).

The structures of the prepared HA MNs containing CS–MoS_2 were analyzed using optical microscopy and SEM. As shown in Fig. 3, it could be seen from the images taken using a mobile phone that the prepared MNs had a square structure and the backing of the needle tip was complete. The MN tips observed from different angles under an optical microscope had a complete tip morphology and uniform distribution. The magnified microstructure of the prepared MNs was further observed with a SEM. According to the obtained images, it could be seen that the prepared HA MNs had an obvious quadrangular pyramidal needle tip structure and good needle shape, indicating that the selected matrix prescription could produce an MN patch with a good morphology.

To prove that CS–MoS_2 was indeed contained in the MNs, elemental scanning was carried out on CS–MoS_2 MNs, and the local image after amplification of the MNs is shown in Fig. 4, which showed the corresponding nanostructures. The elemental mapping results showed that there were corresponding elemental distributions for, C, N, O, S, and Mo on the dissolving HA MNs containing CS–MoS_2 (Fig. 4b–f), indicating that the dissolving HA MNs containing CS–MoS_2 were successfully prepared.

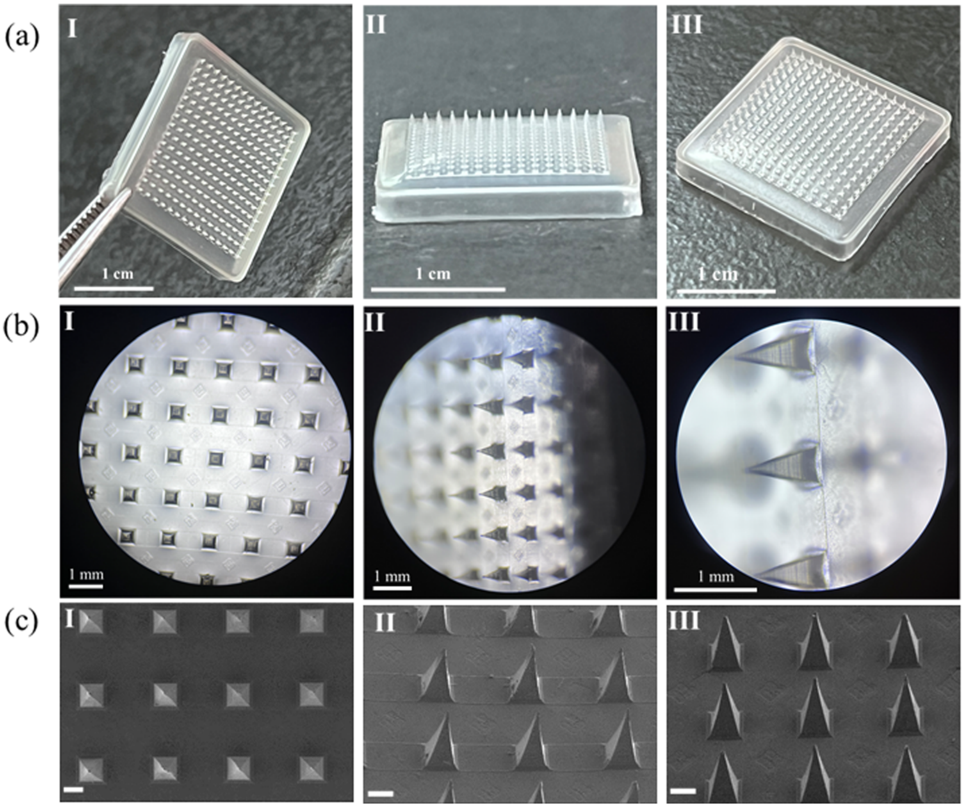

Fig. 3 Morphological characterization images of dissolving HA MNs containing CS–MoS_2. The direct view of the MNs taken using a mobile phone (a); the shape of the MN tips under an optical microscope (b); the SEM images of the dissolving HA MNs containing CS–MoS_2 (c), scale bars: 200 μm.

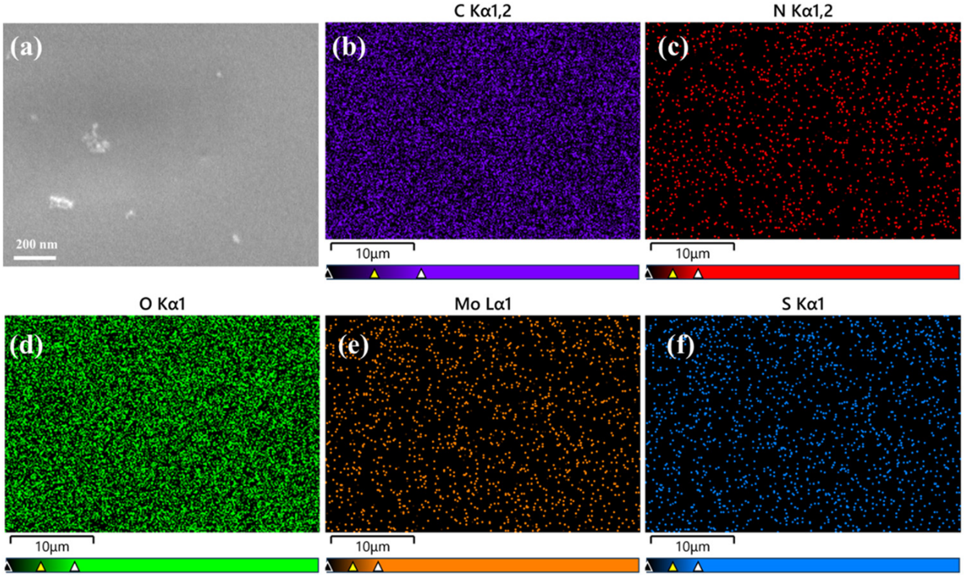

Fig. 4 SEM image of dissolving HA MNs containing CS–MoS_2 (a) and the corresponding elemental mapping for C (b), N (c), O (d), Mo (e), and S (f) dissolving HA MNs containing CS–MoS_2.

3.2. FTIR

The presence of CS and Mo^{4+} in CS–MoS_2 was characterized by FTIR.[37,38] FTIR spectroscopy was used to assess the functional groups present in the polymer structure by detecting the bands of tensile and bending vibrations. The FTIR spectra of CS, MoS_2, and CS–MoS_2 nanocomposites are shown in Fig. 5d. The pure CS spectrum showed two characteristic bands centered at 1656 and 1598 cm^{-1}, corresponding to the stretching vibration of C═O in –NHCO and the bending vibration of an N–H single bond in H–NH_2, respectively; the broad and strong absorption peak near 3431 cm^{-1} could be attributed to the symmetrical stretching vibration of the hydroxyl group; the peak at 2800–3000 cm^{-1} was attributed to the –CH_2 single bond, and 1381 cm^{-1} was attributed to the stretching of the C–N bond mode, the band at 1000–1200 cm^{-1} was attributed to the stretching vibration of the C–O single bond. In the FTIR spectra of MoS_2, a broad stretching band centered on –OH could be observed at around 3440 cm^{-1}, in addition, the spectrum showed a unique peak of Mo–S single-bond vibrations located at around 467 cm^{-1}. Compared with pure CS and MoS_2, the FTIR spectrum of the CS–MoS_2 hybrid nanocomposite exhibited a broad peak at 3422 cm^{-1}, corresponding to the OH stretching vibration of single-bond hydroxyl groups. The peak at 1598 cm^{-1} related to the absorption vibration of NH disappears in the spectrum of the CS–MoS_2 nanocomposite. The CS–MoS_2 composite had a peak at 1408 cm^{-1}, corresponding to the –CH_3 symmetrical deformation, which was different from those of pristine CS and MoS_2. The peak at 1078 cm^{-1} was ascribed to the single-bond CO skeleton stretching vibration. The out-of-plane deformation vibrations at around 700 cm^{-1} were assigned to the bands of N–H single bonds or C–H single bonds, respectively. Furthermore, all peaks were shifted towards the wavelet number compared to the original CS. The above facts could be attributed to the electrostatic interaction between the CS and the negative charges on the MoS_2 surface.

3.3. Zeta potential analysis, XRD and UV-visible spectroscopy

The CS, MoS_2, and CS–MoS_2 nanocomposites were formulated into appropriate concentration solutions using the same solvent and their zeta potential values were measured respectively to preliminarily confirm surface functionalization. Fig. 5f showed that MoS_2 had a negative zeta potential of −21 mV, CS had a positive zeta potential of 45.9 mV, and CS–MoS_2 had a positive zeta potential of 31.7 mV, indicating that the positively charged CS was functionalized on MoS_2.

The crystal structure of CS–MoS_2 was analyzed by powder X-ray diffraction (XRD), and the patterns were recorded in the 2θ range of 10–80° with a scanning speed of 10°/min. The original MoS_2 showed several obvious diffraction peaks in the measured range (14.42°, 28.94°, 32.7°, 33.46°, 36.04°, 39.52°, 44.18°, 49.86°, 58.48°, and 60.44°, respectively). The original chitosan had an obvious peak at 19.9° and a weak peak at 29.48° and 30.94°. After loading MoS_2, the intensity of the diffraction peak of chitosan decreased obviously due to the high-intensity diffraction peak of MoS_2. It was proved that chitosan was successfully functionalized on the MoS_2 surface, and CS–MoS_2 nanocomposites were formed. The X-ray diffraction patterns of synthesized MoS_2 and CS–MoS_2 are shown in Fig. 5e. However, the diffraction peak of CS–MoS_2 was very weak, which was presumed to be due to the weak force of CS and MoS_2.

The synthesized nanocomposites were characterized by UV-Vis spectroscopy, Fig. 5a–c shows the UV-Vis absorption spectrum of CS–MoS_2 (a), CS (b), and MoS_2 (c). All three exhibited obvious absorption spectra, but slightly different absorption peaks. Based on the inherent polysaccharide structure, CS (Fig. 5b) showed an absorption maximum at about 255 nm. MoS_2 nanosheets (Fig. 5c) showed four transition peaks at 339, 383, 640, and 680 nm. The UV-Vis absorption of CS–MoS_2 hybrid nanocomposites (Fig. 5a) fell at 290 and 340 nm due to the complexation of 2D metal nanomaterials

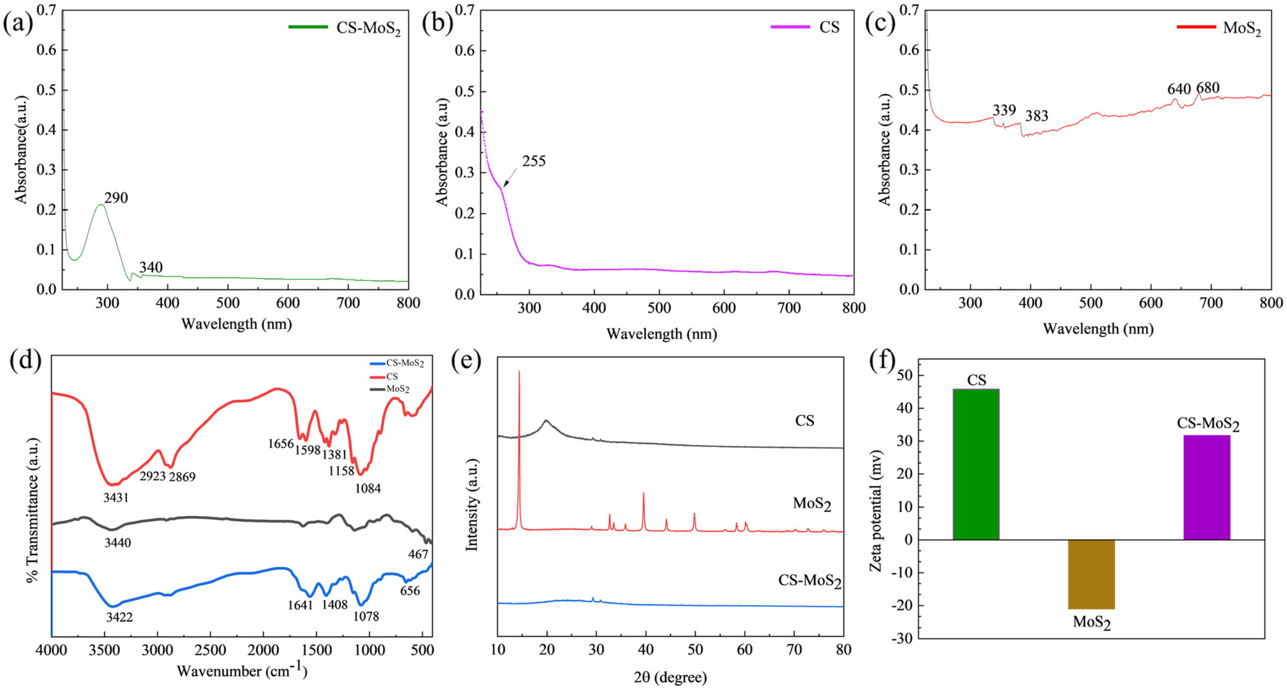

Fig. 5 The UV-Vis absorption (a–c), FTIR (d), XRD (e) and zeta potential (f) spectra of CS, MoS_2 and CS–MoS_2.

and the natural carbohydrate material CS. If the CS–MoS_2 complex is synthesized by a method that can better functionalize CS and make the group binding more stable, it is speculated that this method can be used for quantitative detection and analysis.[32]

3.4. Mechanical property investigation

The mechanical properties of the MNs were evaluated by piercing the MNs into the aluminum foil and observing the condition of the holes left by the piercing with light (Fig. 6a–d). The force applied when studying the mechanical properties of

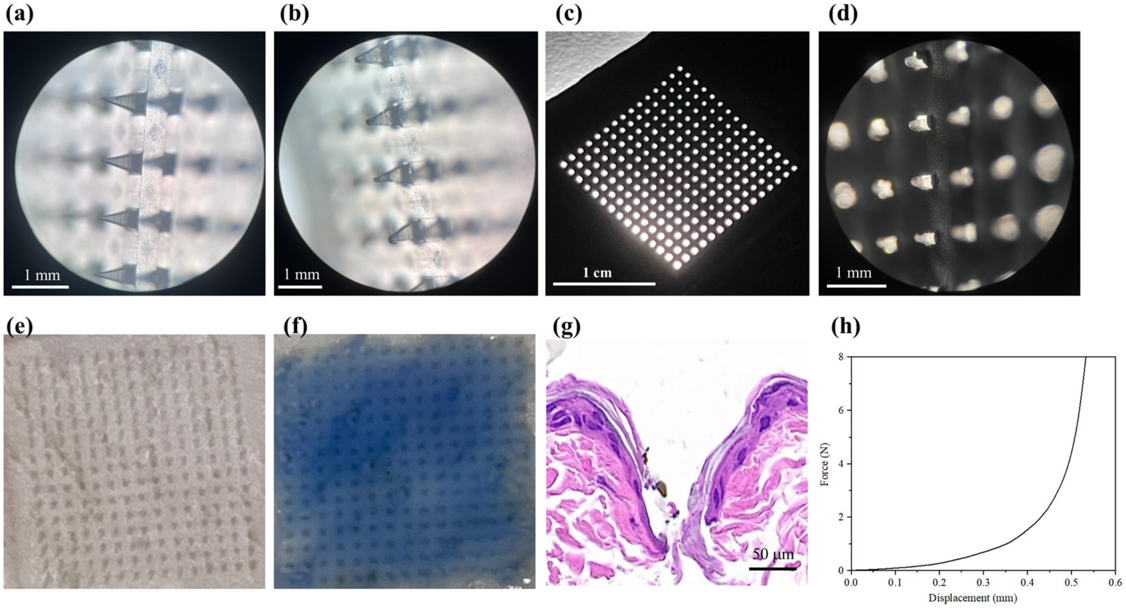

Fig. 6 Optical micrograph (a) of the original dissolving HA MN tips; the optical microscopy image of the MN tips after inserting the aluminum foil (b); the aluminum foil after inserting the MNs (c); the image under the microscope when the MNs were inserted into the aluminum foil (d); the state of the holes left after HA MNs were inserted into pigskin (e, original; f, stained); H&E-stained cross-section of rat skin treated with MN (g); force–displacement curve of the prepared dissolving MNs (h).

microneedles with aluminum foil is consistent with the force applied to the rat skin. Fig. 6a shows the morphology of the original needle tips under an optical microscope, and Fig. 6c shows the pinhole left on the aluminum foil after the insertion of the MNs. By observing the morphology of the tips of the MN before and after the insertion of the aluminum foil under a microscope, it could be seen that the prepared MN has good mechanical properties. It was hard enough to break the aluminum foil and maintain a good shape of the tip after the aluminum foil was inserted, and the tip was only slightly bent without breaking the needles (Fig. 6b and d).

The compression test of the prepared MN was carried out by using the electronic universal testing machine to further investigate the mechanical properties of the MN. The relationship between force and displacement is shown in Fig. 6h. The results showed that with the increase of pressure, the tip of the MN gradually bent. It was speculated that the prepared MN could withstand the pressure of 2–3 N and meet the need for penetrating into the skin (about 1.5 N).[39]

3.5. Skin puncture test

The thawed pork skin was spread on the filter paper with the cuticle facing outwards, the MN was pressed vertically with a certain force for 30 s, and the MN was removed. Fig. 6e shows the unstained pores and Fig. 6f shows the stained pores; it was easy to distinguish whether the holes were the pores of the pig itself or were left by the penetration of MNs. After the trypan blue solution was removed from the skin surface, the pinholes formed by MNs in the pig skin were clearly visible. Then the holes left on the surface of the pig skin were counted, and the puncture rate was calculated to be about 98% according to the formula mentioned in 2.6.3, indicating that the MNs had good mechanical properties.

The MN was inserted into the back skin of the rats and H&E staining was performed on the puncture site to further evaluate the penetration of the MN into the skin. The staining results are shown in Fig. 6g, which confirmed that the epidermis was successfully broken by the MN without inflammation.

3.6. Skin healing test

The skin healing at the puncture site of MN was evaluated using pig skin *in vitro* and rat skin *in vivo*. Experiments were performed according to the procedures described in 2.6.4 and photographed for recording. As shown in Fig. S4a (ESI†), the healing time of MNs on pig skin *in vitro* was 30 min. In addition, according to Fig. S4b (ESI†), as time went on, the holes formed by MNs on the skin of living rats gradually healed and disappeared within 10 min. No adverse reactions such as redness, swelling, and inflammation were observed on the skin surface of rats, and the healing condition was good.

3.7. Solubility study

The *in vitro* and *in vivo* dissolution of the MNs was investigated. Fig. 7a shows the dissolution of MNs when inserted into pig skin. It could be seen that the thawing of the isolated pig skin with normal saline resulted in increased moisture in the pig skin, so the dissolving MNs dissolved rapidly on the pig skin. Fig. 7b shows the dissolution of MN tips after insertion into rats for different periods. According to the results of optical microscopy images, the dissolution rate of dissolving HA MNs after insertion into intact rat skin was slower than that in pig skin with more water content, but the MNs could still be dissolved within 10 min, thus achieving rapid local administration.

3.8. Blood compatibility test

The procedure for the hemolysis assay of nanocomposites and MN patches followed published methods.[40] To evaluate the blood compatibility of the prepared MN patches, a hemolysis experiment was performed according to the steps described in 2.6.5 and the hemolysis rate was calculated. The results showed that the hemolysis rate of each experimental group was far less than 5%, indicating that the antibacterial MN patch loaded

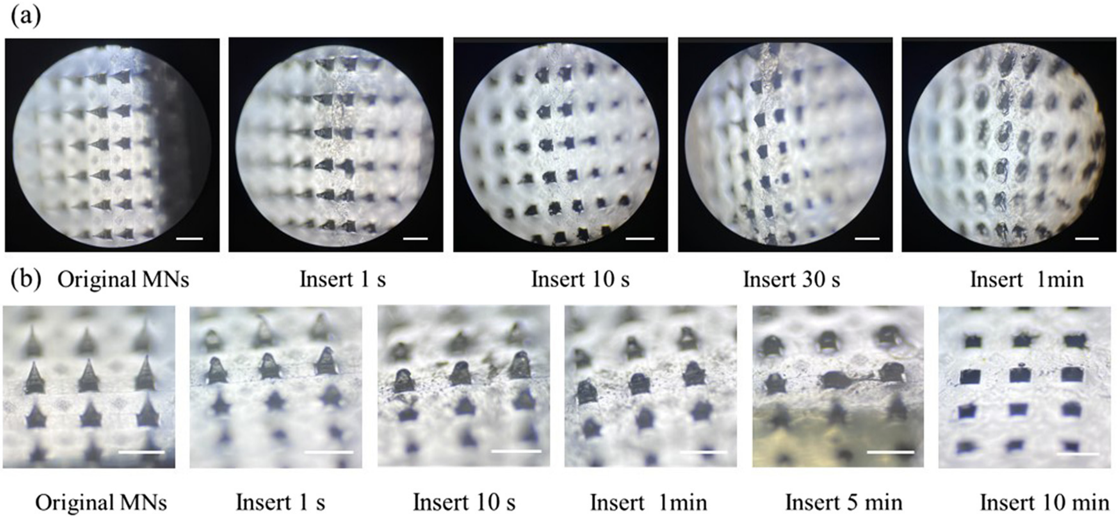

Fig. 7 Dissolution of dissolving HA MNs in isolated porcine skin (a); dissolution of dissolving HA MNs in rat skin (b). Scale bars: 1 mm.

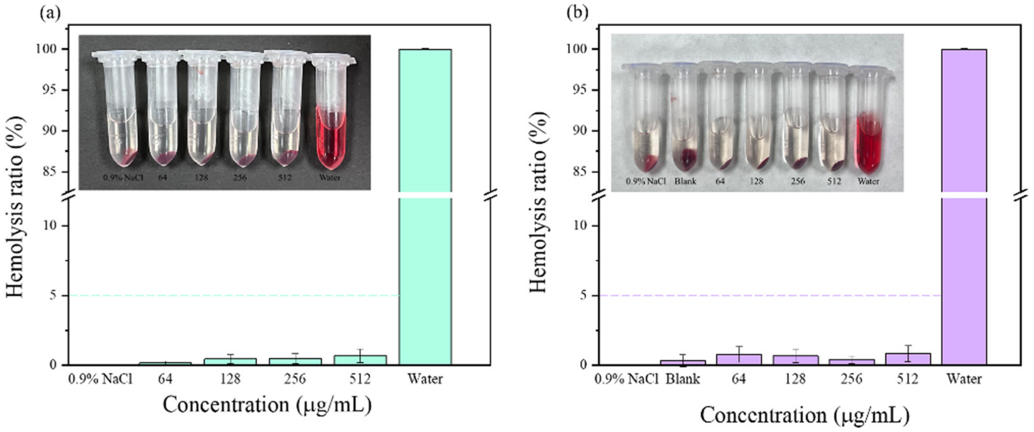

Fig. 8 Hemolysis ratio of CS–MoS_2 (a) and MNs loaded with CS–MoS_2 (b).

with the CS–MoS_2 complex had good blood compatibility. The hemolysis rate of nanocomposites and MN patches is shown in Fig. 8.

3.9. Antibacterial performance evaluation

3.9.1. MIC&MBC. Nanocomposites generated from the combination of a naturally derived biopolymer CS and a layered (2D) material MoS_2 are potential new antibacterial materials because layered materials have the advantages of large surface areas, low toxicity, good biodegradability, and potential biomedical applications.

The MIC and MBC of the CS–MoS_2 complex against *S. aureus* and *E. coli* were investigated by the double dilution method. The results demonstrated that the MIC and MBC of the CS–MoS_2 complex against *S. aureus* and *E. coli* were 128, 256 μg mL^{-1} and 64, 128 μg mL^{-1} (Fig. S5, ESI†), respectively.

3.9.2. Comparison of the antibacterial activity of CS, MoS_2, and CS–MoS_2. The three groups of the samples for comparison were set at the same concentration according to the growth of bacteria on an agar plate as described in section 3.9.1 (128 μg mL^{-1} for *S. aureus* and 64 μg mL^{-1} for *E. coli*). The results showed that CS–MoS_2 nanocomposites had a higher antibacterial effect on *S. aureus* and *E. coli* than CS and MoS_2 alone (Fig. 9).

3.9.3. Sterilizing rate of CS–MoS_2 MNs. The MNs were co-cultured with the bacterial solution as described in section 2.7, and the growth conditions of the two bacteria co-cultured with MNs carrying different concentrations of CS–MoS_2 are shown in Fig. 10a and b. The images showed that the antibacterial effect of drug-loaded MNs increased with the increase of the CS–MoS_2 concentration. The plate counting method was used to count the viable bacteria and calculate the sterilization rate and the results are shown in Table 1. When the concentration of CS–MoS_2 was 64 μg mL^{-1}, 128 μg mL^{-1}, 256 μg mL^{-1}, and 512 μg mL^{-1}, the sterilization rate of the MN patch containing the corresponding concentration of CS–MoS_2 to *E. coli* and *S. aureus* was 80.74%, 97.50%, 99.56%, and 100.00% and 49.01%, 82.23%, 96.25%, and 99.75%, respectively. The corresponding bacterial survival rate was plotted in a bar chart (Fig. 10c and d). The results showed that when a certain concentration of CS–MoS_2 was added to MNs according to the

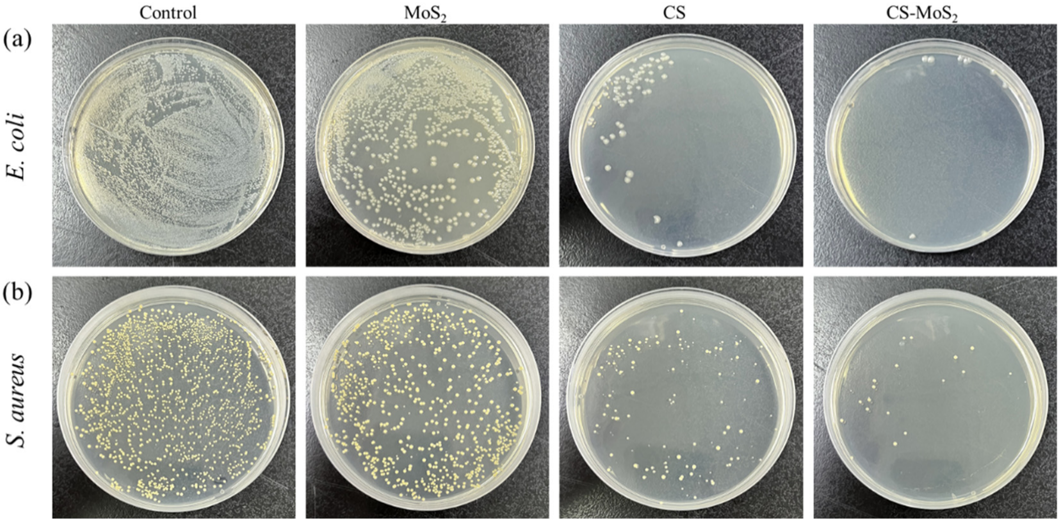

Fig. 9 Digital images of *E. coli* (a) and *S. aureus* (b) cultured with CS, MoS_2, and CS–MoS_2.

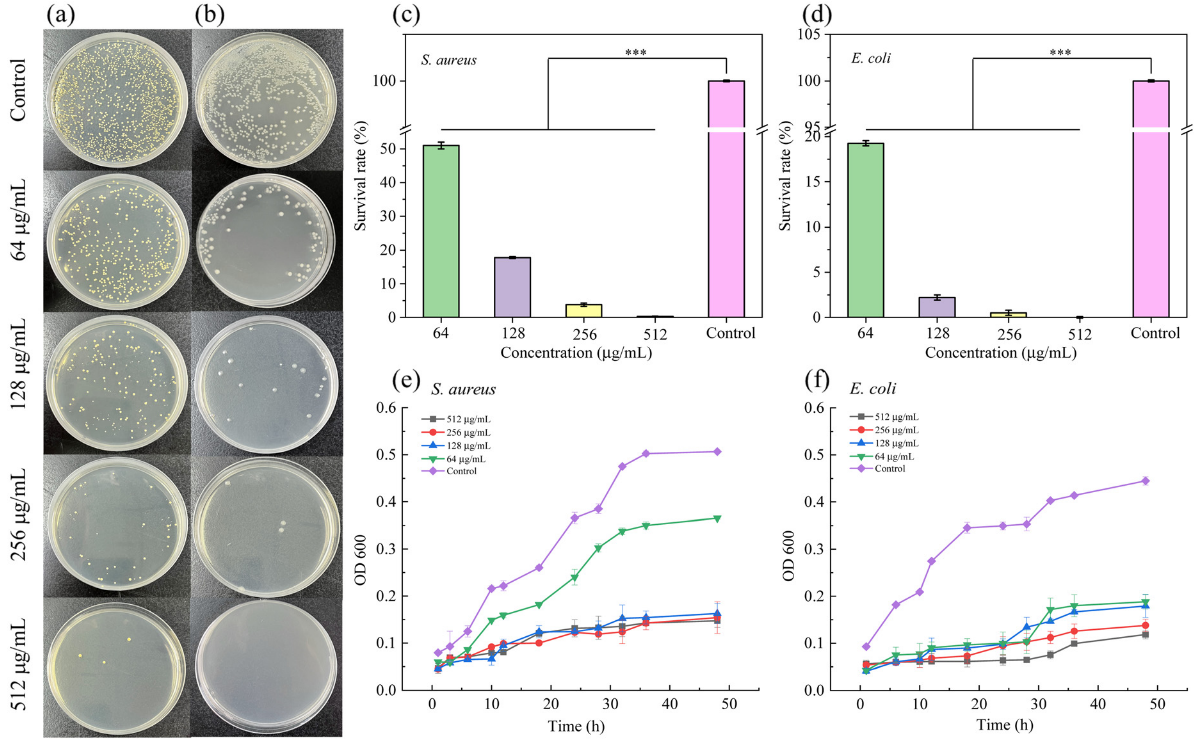

Fig. 10 The sterilization rate of HA MNs containing different concentrations of CS–MoS_2 against *S. aureus* and *E. coli* (a and b); the corresponding survival rate of the bacteria (c and d); the growth curves of MNs containing different concentrations of CS–MoS_2 against *S. aureus* (e) and *E. coli* (f).

MIC and MBC, the antibacterial activity of the same concentration of antimicrobial agents against bacteria decreased. The inhibitory effect of the MN patch on *E. coli* was better than that of *S. aureus*. This part of the experiment showed that in order to achieve the ideal antibacterial effect, it was necessary to increase the concentration of CS–MoS_2 when adding to the MN patches to achieve a good antibacterial effect.

3.9.4. Growth curves. Antibacterial experiments were performed by immersing CS–MoS_2-loaded MN patches in *S. aureus* and *E. coli* bacterial solutions to evaluate the antibacterial properties of MN patches. A quarter of MN containing 512 μg mL^{-1} of CS–MoS_2 was added into 100 μL of bacterial suspension (10^7 CFU mL^{-1}), then 400 μL of medium for the growth of bacterial solution and 500 μL of normal saline for dilution was added to obtain an MN and bacterial solution (10^6 CFU mL^{-1}) co-culture system. The addition of normal saline could effectively prevent the influence of the gel formed by MNs on the treatment of the measured solution. In the experimental group, MN patches with different concentrations of CS–MoS_2 were immersed in the culture solution containing bacteria, and the control group was a bacterial solution without MN patches. The bacterial suspensions of *E. coli* and *S. aureus* were co-cultured with the MN patches of the experimental group in a constant temperature shaker at 37 °C, and the optical density (OD 600) values of the cultured bacteria were measured at different times, and the growth curves are shown in Fig. 10e and f. The growth curves demonstrated that the OD 600 values of *S. aureus* and *E. coli* in the control group showed a steady increase and gradually tended to be flat during the investigation period.

The results showed that different concentrations of CS–MoS_2 MNs had certain antibacterial effects compared with the control group. With the increase of the CS–MoS_2 concentration, the antibacterial effect was enhanced. For the two strains, MNs containing different concentrations of CS–MoS_2 had different antibacterial effects. There was an obvious difference between the experimental group and the control group within 20 h. For *E. coli*, there was no obvious difference between the four concentrations of MNs, while 512 μg mL^{-1} was the best. For *S. aureus*, MNs with a CS–MoS_2 concentration of 64 μg mL^{-1} had no obvious antibacterial effect, while the other three concentrations of MNs had a better antibacterial effect.

The antibacterial mechanism of the CS–MoS_2 nanocomposites is mainly due to oxidative stress on the bacterial cell membrane that destroys DNA in the bacterial system, and the nano-sized CS–MoS_2 nanocomposites penetrate the cell membrane and cause damage to the interior of bacterial cells. Furthermore, the antibacterial effect can also be attributed to the release of metal cations (Mo^{4+}) and non-metal anions (S^{2-}) in the CS–MoS_2 nanocomposites. The released cations are taken up by the bacteria. The adsorbed cations bind to the phospholipid surface of the bacterial system, resulting in the release of the cellular material from the bacteria. *E. coli* has a thin layer of proteins and lipids in its structure, so the metal ions in CS–MoS_2 can permeate and damage the DNA of the bacterial system easily. Therefore, compared with *S. aureus*, the MN patch containing CS–MoS_2 has a better inhibitory effect on *E. coli*.

Table 1 Coculture results of *S. aureus* and *E. coli* co-cultured with different concentrations of CS–MoS_2 MNs

Concentration of CS–MoS_2		64 μg mL^{-1}	128 μg mL^{-1}	256 μg mL^{-1}	512 μg mL^{-1}	Control
S. aureus	The number of colonies	612	212	45	3	1200
	Sterilization rate	49.01%	82.23%	96.25%	99.75%	100%
	Survival rate	50.99%	17.77%	3.75%	0.25%	0%
E. coli	The number of colonies	131	17	4	0	680
	Sterilization rate	80.74%	97.50%	99.56%	100.00%	100%
	Survival rate	19.26%	2.5%	0.44%	0%	0%

3.10. Wound healing experiment

According to the experimental results presented in section 3.9.3, the appropriate concentration of MNs should be increased when used in *in vivo* experiments. Therefore, 512 μg mL^{-1}, which has been verified to have good blood compatibility, was used to prepare MNs for the back wounds of rats in the wound healing experiment. During the process of wound healing, pictures of wounds were taken at different times for comparison. The images of wounds on days 0, 3, 5, 7, 9 and 14 are shown in Fig. 11a and b. Then the wound area at different times was calculated to obtain the healing rate. As shown in Fig. 11c, on the ninth and fourteenth days, the wound healing rates of the control group and the experimental group were 33.03%, 71.04% and 66.15%, 89.15%, respectively.

Furthermore, the degree of regenerative epithelialization was used to evaluate wound repair.[41] In order to better show the different degrees of healing between the experimental group and the control group, H&E staining was performed on the skin at the molding sites of the two groups of rats when the experimental group was almost completely healed, and the results were shown in Fig. 11d. The results showed that a large number of necrotic cell fragments (black arrow) and hemorrhage (yellow arrow) were seen in the injured area of the control group. However, there was no obvious new epidermis at the edge of the injured area. In contrast, the injured areas of the experimental group treated with CS–MoS_2 MNs showed the newly formed epidermis (brown arrow) and stratum corneum (orange arrow). The dermis and subcutaneous muscle layer were repaired by hyperplastic scar tissue and fibrous cells, as well as collagen fibers secreted by them, accompanied by new blood vessels (blue arrow), and no bleeding was found. The results of *in vivo* wound healing experiments showed that the MNs prepared in our study had a potential role in promoting wound healing.

4. Conclusion

In this study, antibacterial nanocomposites containing CS and MoS_2 were synthesized with superior bactericidal efficacy over the original materials. After the prepared nanocomposites were mixed into the HA matrix to make MNs, the MN samples

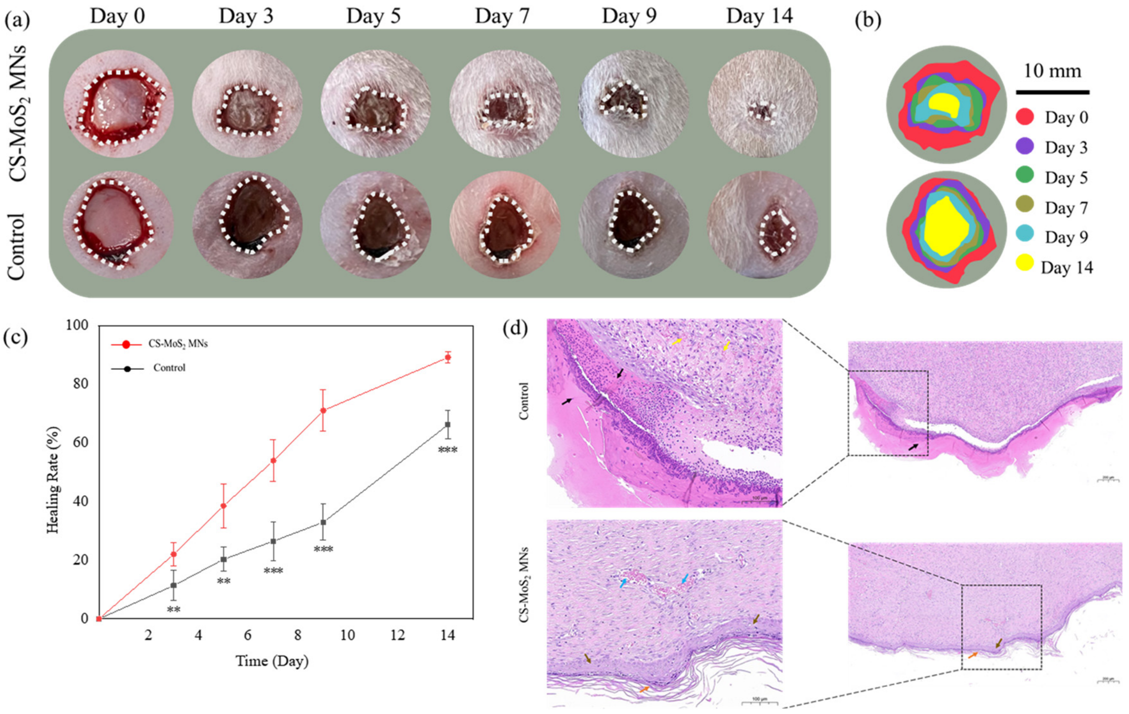

Fig. 11 Wound images of the control and experimental groups on days 0, 3, 5, 7, 9, and 14 (a); schematic diagram of the wound size in the two groups during the experimental time (b); the wound healing rate of the two groups (c); H&E histological analysis of regenerated skin tissue in the control group and experimental group after 14 days of treatment (d); significances are presented by $^{*}p < 0.1$, $^{**}p < 0.05$, and $^{***}p < 0.01$.

showed good mechanical properties. The MNs further showed good blood compatibility and good dissolution properties on the skin. The good recovery ability indicated that the CS–MoS_2 nanocomposite-loaded HA MNs exhibited mild skin irritation. The results of growth curves showed that the dissolving MNs had a good inhibitory effect on bacterial growth. The MNs prepared based on biocompatible carbohydrates HA and CS combined with metal nanomaterials had good antibacterial properties. The preliminary study through this experiment showed that the proposed nanocomposite MNs could be an interesting candidate material for biomedicine, and further research could replace the method of synthesizing a nanocomposite so that the synthesized nanocomposite might have better antibacterial properties and thus reduce the MIC & MBC. The MNs studied in this experiment had similar self-disinfection properties and had potential biomedical application value.

Ethics approval statement

All the animal experiments involved in this experiment were following the animal experiment ethical review method of Shenyang Pharmaceutical University.

Author contributions

Wenzhen Du: conceptualization, methodology, investigation, writing – original draft, and formal analysis. Xiaodan Li: writing – review & editing. Manyue Zhang: writing – review & editing. Guixia Ling: resources and writing – review & editing. Peng Zhang: resources, writing – review & editing, and supervision.

Conflicts of interest

There are no conflicts of interest to declare.

Acknowledgements

This research did not receive any specific grant from funding agencies in the public, commercial, or not-for-profit sectors.

References

1 S. B. Levy and B. Marshall, *Nat. Med.*, 2004, **10**, S122–S129.
2 A. M. Allahverdiyev, K. V. Kon, E. S. Abamor, M. Bagirova and M. Rafailovich, *Expert Rev. Anti-Infect. Ther.*, 2011, **9**, 1035–1052.
3 A. J. Huh and Y. J. Kwon, *J. Controlled Release*, 2011, **156**, 128–145.
4 W. Du, Q. Zong, R. Guo, G. Ling and P. Zhang, *Macromol. Biosci.*, 2021, **21**, e2100186.
5 W. Du, L. Zhang, X. Li, G. Ling and P. Zhang, *Int. J. Pharm.*, 2022, **619**, 121735.
6 V. Yadav, S. Roy, P. Singh, Z. Khan and A. Jaiswal, *Small*, 2019, **15**, e1803706.
7 Z. Feng, X. Liu, L. Tan, Z. Cui, X. Yang, Z. Li, Y. Zheng, K. W. K. Yeung and S. Wu, *Small*, 2018, **14**, e1704347.
8 V. Yadav, S. Roy, P. Singh, Z. Khan and A. Jaiswal, *Small*, 2019, **15**, e1803706.
9 Q. Gao, X. Zhang, W. Yin, D. Ma, C. Xie, L. Zheng, X. Dong, L. Mei, J. Yu, C. Wang, Z. Gu and Y. Zhao, *Small*, 2018, **14**, e1802290.
10 V. Agarwal and K. Chatterjee, *Nanoscale*, 2018, **10**, 16365–16397.
11 M. Chhowalla, H. S. Shin, G. Eda, L. J. Li, K. P. Loh and H. Zhang, *Nat. Chem.*, 2013, **5**, 263–275.
12 X. Yang, J. Li, T. Liang, C. Ma, Y. Zhang, H. Chen, N. Hanagata, H. Su and M. Xu, *Nanoscale*, 2014, **6**, 10126–10133.
13 W. Cao, L. Yue and Z. Wang, *Carbohydr. Polym.*, 2019, **215**, 226–234.
14 Z. Feng, X. Liu, L. Tan, Z. Cui, X. Yang, Z. Li, Y. Zheng, K. W. K. Yeung and S. Wu, *Small*, 2018, **14**, e1704347.
15 W. Yin, J. Yu, F. Lv, L. Yan, L. R. Zheng, Z. Gu and Y. Zhao, *ACS Nano*, 2016, **10**, 11000–11011.
16 W. Zhang, S. Shi, Y. Wang, S. Yu, W. Zhu, X. Zhang, D. Zhang, B. Yang, X. Wang and J. Wang, *Nanoscale*, 2016, **8**, 11642–11648.
17 H. Shen, C. Jiang, W. Li, Q. Wei, R. A. Ghiladi and Q. Wang, *ACS Appl. Mater. Interfaces*, 2021, **13**, 31193–31205.
18 K. Jung, N. Corrigan, E. H. H. Wong and C. Boyer, *Adv. Mater.*, 2022, **34**, e2105063.
19 K. Yin, P. Divakar and U. G. K. Wegst, *Acta Biomater.*, 2019, **84**, 231–241.
20 M. Zhao, Z. Huang, S. Wang and L. Zhang, *Chem. Eng. J.*, 2020, **401**, 126006.
21 Y. Huang, Q. Gao, X. Li, Y. Gao, H. Han, Q. Jin, K. Yao and J. Ji, *Nano Res.*, 2020, **13**, 2340–2350.
22 T. M. Tuan-Mahmood, M. T. McCrudden, B. M. Torrisi, E. McAlister, M. J. Garland, T. R. Singh and R. F. Donnelly, *Eur. J. Pharm. Sci.*, 2013, **50**, 623–637.
23 Y. Ye, J. Yu, C. Wang, N. Y. Nguyen, G. M. Walker, J. B. Buse and Z. Gu, *Adv. Mater.*, 2016, **28**, 3115–3121.
24 L. Yang, Y. Yang, H. Chen, L. Mei and X. Zeng, *Asian J. Pharm. Sci.*, 2022, **17**, 70–86.
25 M. Wu, T. Xia, Y. Li, T. Wang, S. Yang, J. Yu, Q. Liang, T. Shen, M. Yu and B. Zhao, *Asian J. Pharm. Sci.*, 2022, **17**, 284–297.
26 L. Zhang, R. Guo, S. Wang, X. Yang, G. Ling and P. Zhang, *Int. J. Pharm.*, 2021, **604**, 120749.
27 A. Than, C. Liu, H. Chang, P. K. Duong, C. M. G. Cheung, C. Xu, X. Wang and P. Chen, *Nat. Commun.*, 2018, **9**, 4433.
28 Q. Zong, R. Guo, N. Dong, G. Ling and P. Zhang, *Drug Delivery Transl. Res.*, 2022, **12**, 973–980.
29 S. Gao, W. Zhang, X. Zhai, X. Zhao, J. Wang, J. Weng, J. Li and X. Chen, *Biomater. Sci.*, 2023, **11**, 533–541.
30 X. Lei, M. Li, C. Wang, P. Cui, L. Qiu, S. Zhou, P. Jiang, H. Li, D. Zhao, X. Ni, J. Wang and J. Xia, *Int. J. Biol. Macromol.*, 2022, **217**, 55–65.
31 Y. Shi, J. Zhao, H. Li, M. Yu, W. Zhang, D. Qin, K. Qiu, X. Chen and M. Kong, *Adv. Healthcare Mater.*, 2022, **11**, e2200908.
32 K. Kasinathan, B. Murugesan, N. Pandian, S. Mahalingam, B. Selvaraj and K. Marimuthu, *Int. J. Biol. Macromol.*, 2020, **149**, 1019–1033.
33 K. J. Huang, Y. J. Liu, Y. M. Liu and L. L. Wang, *J. Hazard. Mater.*, 2014, **276**, 207–215.

34 X. Feng, X. Wang, W. Xing, K. Zhou, L. Song and Y. Hu, *Compos. Sci. Technol.*, 2014, **93**, 76–82.

35 X. Chao, C. Zhang, X. Li, H. Lv, G. Ling and P. Zhang, *Biomater. Sci.*, 2022, **10**, 1008–1017.

36 X. Zhao, H. Wu, B. Guo, R. Dong, Y. Qiu and P. X. Ma, *Biomaterials*, 2017, **122**, 34–47.

37 J. Ruan, X. Wang, Z. Yu, Z. Wang, Q. Xie, D. Zhang, Y. Huang, H. Zhou, X. Bi, C. Xiao, P. Gu and X. Fan, *Adv. Funct. Mater.*, 2016, **26**, 1085–1097.

38 G. Lawrie, I. Keen, B. Drew, A. Chandler-Temple, L. Rintoul, P. Fredericks and L. Grøndahl, *Biomacromolecules*, 2007, **8**, 2533–2541.

39 S. W. T. Chew, Y. Zeng, M. Cui, H. Chang, M. Zheng, S. Wei, W. Zhao and C. Xu, *SLAS Technol.*, 2019, **24**, 181–187.

40 C. Zhou, C. Sheng, L. Gao, J. Guo, P. Li and B. Liu, *Chem. Eng. J.*, 2021, **413**, 127429.

41 S. Yao, J. Chi, Y. Wang, Y. Zhao, Y. Luo and Y. Wang, *Adv. Healthcare Mater.*, 2021, **10**, e2100056.